Achieving 0.3 millisecond coherence in scalable aluminum transmon qubits through surface engineering

Neha Mahuli,* Joaquin Minguzzi, Jiansong Gao, Cliff Chen, David Perello, Rachel Resnick,† Sandra Diez,‡ Shahriar Aghaeimeibodi, Cosmic Raj, Guillaume Marcaud, Matthew Hunt, Loren Swenson, Jefferson Rose, Oskar Painter, and Ignace Jarrige§
AWS Center for Quantum Computing, Pasadena, CA 91106, USA
(Dated: April 2, 2025)

We present a dry surface treatment combining atomic layer etching and deposition (ALE and ALD) to mitigate dielectric loss in fully fabricated superconducting quantum devices. The treatment starts by conformally removing the native metal oxide and fabrication residues from the exposed surfaces through ALE before *in situ* encapsulating the metal surfaces with a thin dielectric layer using ALD. We measure a two-fold reduction in loss attributed to two-level system (TLS) absorption in treated aluminum-based resonators and planar transmon qubits. Transmons with compact capacitor plates and gaps achieve 90^{th} percentile Q values of 6 M, translating to T_1 values of 320 μs at 3 GHz. These improvements were found to be sustained over several months. We discuss how the combination of ALE and ALD reverses fabrication-induced surface damages to significantly and durably improve device performance via a reduction of the TLS defect density in the capacitive elements.

I. INTRODUCTION

Superconducting transmons are a leading platform for building a scalable, fault-tolerant quantum computer capable of solving problems currently intractable with classical computing architecture[1]. In the early stages of development, transmon performance improved primarily through design optimizations, such as reducing dielectric participation in critical surfaces[2, 3], minimizing noise sensitivity, and enhancing readout via Purcell filtering. More recently, the focus has shifted toward enhancing the quality of materials, a strategy that has already shown great promise in mitigating two-level system (TLS) losses and improving transmon coherence times[4–7]. Recent studies following this strategy have centered on three primary approaches to reduce the density of TLS defects in the constituent materials: (i) exploring new ground-layer materials that form low-loss native oxides[5, 8], (ii) chemically etching defect-rich surface layers [9–12], and (iii) capping the top surface of the ground layer with low-loss materials [13–17].

Among the main dielectric regions in superconducting circuits, the metal-air (MA) and substrate-air (SA) interfaces are particularly susceptible to degradation during the fabrication process[18]. These interfaces are indeed often characterized by polymeric residues, interstitial contaminants, morphological damages, and thickened oxide layers. This stresses the need to develop post-fabrication surface treatment methods that alleviate or eliminate these effects without introducing new damage. Recent efforts to reduce dielectric loss at the MA interface have used a variety of approaches. This includes wet-etch treatments to remove the native oxide, surface capping of the superconducting ground layer with a lower-loss superconductor, or a noble metal to prevent oxidation. In these studies, surface capping was performed on the blanket ground layer prior to fabrication[13–17], as subsequent etching exposed the sidewalls of the superconductor. This caused the resulting dielectric loss in these capped devices to potentially be dominated by the amorphous oxides on the sidewalls.

Here, we present an alternative surface engineering approach that overcomes this limitation by treating all exposed surfaces of fully fabricated devices using a combination of atomic layer etching and deposition (ALE and ALD). Both ALE and ALD rely on a self-limiting, sequential gas-phase surface reaction mechanism to respectively remove and form material layers with monolayer precision and a high conformality compatible with three-dimensional structures. By applying these techniques to aluminum (Al)-based coplanar waveguide (CPW) resonators and planar transmons, fabrication-related contamination of the Al and silicon (Si) substrate surfaces is substantially reduced and the lossy native Al oxide layer is selectively replaced with a thin and stoichiometric Al_2O_3 capping layer. These improvements in the quality of the MA and SA interfaces correlate with halving of the dielectric loss in the resonators and a two-fold increase of the median quality factor (Q) and transmon coherence times (T_1), reaching 90^{th} percentile Q values of 6 M, translating to T_1 values of 320 μs at 3 GHz. These improvements are achieved for several chips, across a frequency range spanning 2.2-4.4 GHz. This study shows that the *in situ* combination of ALE and ALD serves as an effective and scalable surface engineering strategy for superconducting quantum circuits across different architectures and materials.

* Corresponding email address: mahuli@amazon.com
† Current affiliation: Google Research
‡ Current affiliation: National Institute of Standards and Technology
§ Corresponding email address: jarrige@amazon.com

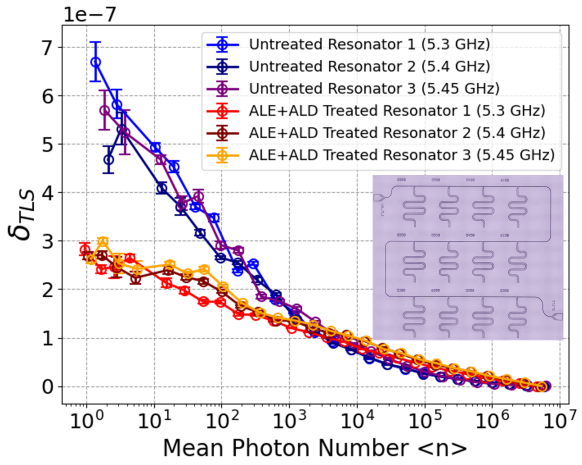

FIG. 1. δ_{TLS} as a function of power for three representative resonators, comparing untreated and ALE+ALD treated samples. Inset: Micrograph of a CPW resonator chip.

II. RESULTS AND DISCUSSION

A. Surface Engineering Effects on Resonator Loss Tangent

Superconducting microwave resonators provide an effective platform for evaluating materials-induced dielectric loss, minimizing the design, fabrication, and measurement overhead compared to transmons[19, 20]. $\lambda/4$ CPW resonators were fabricated using 100 nm thick Al films on high-resistivity silicon substrates, with trace and gap width of 30 μm each ($w_g = w_{tr} = w$). Each chip contains 12 resonators with frequencies ranging from 5.2 to 6.2 GHz, capacitively coupled to the transmission line, as shown in the inset of Figure 1. We performed S_{21} transmission measurements in a dilution refrigerator at a base temperature of 10 mK and the internal quality factors (Q_i) were extracted using a circle-fitting method[21, 22]. Measurements were conducted on untreated devices to establish a baseline, and directly compared with ALE+ALD treated devices.

Our devices exhibit the typical saturation behavior of Q_i as a function of photon number. In the single-photon limit, losses are dominated by unsaturated or slightly saturated TLSs, while at higher power level, Q_i is predominantly limited by other loss mechanisms such as vortices, non-equilibrium quasi-particles, or packaging modes. We quantify the TLS contribution to loss, δ_{TLS}, from high-power (HP) and low-power (LP) Q_i per the following equation [23]:

$$\delta_{TLS} = \frac{1}{Q_{TLS}} = \frac{1}{Q_i^{LP}} - \frac{1}{Q_i^{HP}} \quad (1)$$

Figure 1 shows a power sweep of δ_{TLS} for three untreated/treated pairs of representative resonators at 5.3, 5.4 and 5.45 GHz frequencies. At single-photon powers, the loss of the ALE+ALD treated resonators is approximately half that of the untreated resonators. This shows that materials-based losses can be efficiently reduced in single-layer Al devices using the ALE+ALD treatment.

B. Surface Engineering Effects on Transmon Performance

Motivated by the promising resonator results, we extend our study to transmons made from Al on Si. Here, we compare the quality factor (Q) and relaxation time (T_1) of transmons before and after the treatment. The measurements were conducted on Josephson junction (JJ) based planar transmons coupled to CPW readout resonators. Five chips, each containing four tunable transmons with variable-size junctions and constant-size capacitors (24-μm width, 30-μm gap), were measured in the frequency range of 2.2–4.4 GHz before and after the treatment. Further qubit design details are provided in Table-1 in Supplementary Information (SI). To improve the pre-treatment statistical analysis, six additional untreated chips were measured. One chip was also measured before and after annealing at 300°C under vacuum in the ALD chamber to disentangle the impact of heating from the ALE+ALD treatment, which also takes place at 300°C. Transmon and readout resonator frequencies were measured, and coherence data collected over several hours across a broad frequency range using DC flux pulses for state preparation and readout. This approach enabled us to sample a wider distribution of possible TLS defects, facilitating faster and more accurate characterization of the T_1 distribution[24]. Based on the standard tunneling model (STM)[25], it can be approximated that the TLS density remains constant across the frequency range, allowing us to estimate the transmon quality factor Q as a frequency-independent metric of coherence defined by $Q = 2\pi f_{01} T_1$ [26].

T_1 and Q measurements of treated and untreated transmons are presented in Figure 2(a) and (b), respectively. Across the measured frequency range, Q values remain mainly under 3 M for the untreated control and annealed-only devices and increase to 3-7 M after the treatment, with some values exceeding the 9 M mark. Similarly, most median T_1 times for the untreated and annealed-only devices are below 150 μs, whereas treated devices achieve median T_1 values in the 200–400 μs range.

This improvement can be further quantified by comparing the pre- and post-treatment empirical probability density function (e-PDF) and cumulative distribution function (e-CDF) of a frequency-independent parameter, Q, as shown in Figure 2(c). Prior to the treatment, the e-PDF exhibits a median Q of 1.9 M, while the e-CDF shows a 90^{th} percentile of 2.8 M, which corresponds to a median T_1 of 100 μs and a 90^{th} percentile T_1 of 150 μs for f_{01} of 3 GHz. Following the treatment, the median Q in the e-PDF increases to 3.7 M, while the 90^{th} percentile Q in the e-CDF rises to 6 M, corresponding to a median

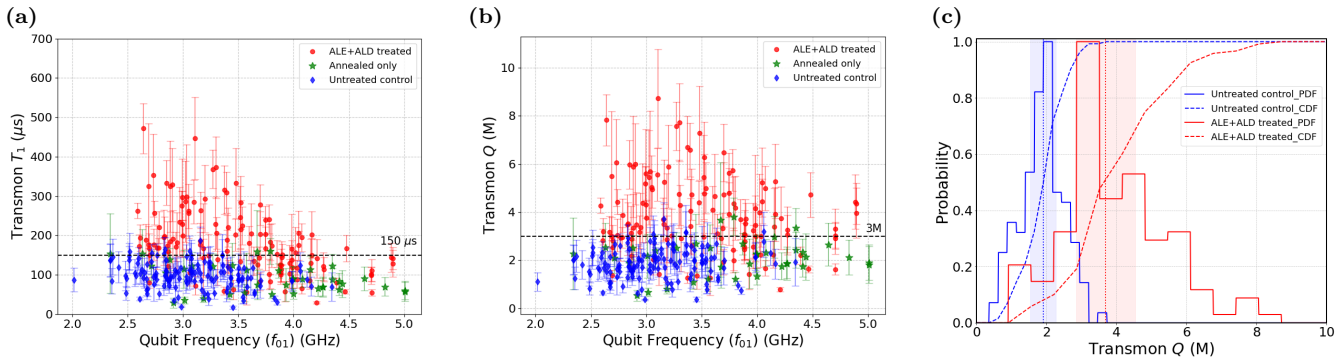

FIG. 2. Frequency dependence of measured T_1 times (a) and estimated Q (b) for various devices as is (untreated), ALE+ALD treated, and annealed-only. The dashed lines are a guide to the eye. The empirical probability distribution function (e-PDF) and cumulative distribution function (e-CDF) are also shown for (c) Q before and after the treatment.

T_1 of 200 μs and 90^{th} percentile T_1 of 320 μs for f_{01} of 3 GHz.

The highest performing treated devices are consistently observed within the 2.6–3.7 GHz range, with some of the Q values surpassing 6 M. The Purcell effect, illustrated in Figure SI-2(a-d), is presumed to contribute to the reduction in T_1 and Q at higher frequencies. Regardless of the Purcell effect, the consistent enhancement in T_1 and Q post-ALE+ALD treatment across the studied frequency range, which is not achieved by annealing alone, provides compelling evidence that the surface dielectric loss of the transmons is reduced by the ALE+ALD treatment specifically. No decline in T_1 and Q was observed in transmons measured over periods of up to 8-9 months after the treatment, highlighting the long-term stability of this treatment.

Additionally, a consistent increase in transmon frequency (f_{01}) by several hundreds of MHz was also observed for all treated transmons (as shown in Figure SI-1). This increase is attributed to junction evolution, as we observe a rise in junction energy (E_j) after the treatment, while capacitive energy (E_c) remains unaffected. This frequency shift is primarily attributed to the elevated processing temperatures during treatment which was also confirmed with annealed-only devices; however, its absolute magnitude is likely influenced by additional factors, such as the initial interface quality before the JJ deposition and fabrication variability. Additionally, we find no correlation between the magnitude of the post-treatment frequency shift and the improvements in Q, as shown in Figure SI-3.

C. Assessing Surface Modifications

The ALE chemistry, utilizing alternating exposures of trimethylaluminum (TMA) and hydrogen fluoride-pyridine (HF-pyridine) at 300°C, was developed to etch the native aluminum oxide. The subsequent ALD process, using TMA and water (H_2O), was tuned to regrow a 1-nm thick Al_2O_3 layer. Detailed process parameters and methodology are provided in the Methods section. Here, we characterize the effect of these processes on the chemical properties of the surface of our devices, using a combination of x-ray photoelectron spectroscopy (XPS), photo-induced force infrared microscopy (PiFM), and transmission electron microscopy complemented by electron energy loss spectroscopy (TEM-EELS). Using lab-scale XPS with an Al Kα x-ray source (λ = 1486.6 eV), we measured the Al 2p, C 1s, and O 1s core levels on the surface of transmon qubit chips. A detailed description of the fitting procedure is provided in SI (Figures SI-4 through 6). To check the consistency of the observed trends, we measured two sites per untreated and annealed-only chip, and a total of four sites on two different treated chips.

The XPS data is shown in Figure 3 for the surfaces of untreated, annealed-only, and ALE+ALD treated transmon qubit chips, and compared with blanket films of ALD-grown Al_2O_3 and evaporated Al. In the fits, up to four characteristic binding energies (BE) can be distinguished for the Al 2p oxide components. Ranked by increasing BE (see 3(a)), these are assigned to native Al oxide, ALD-grown Al_2O_3, post-fabrication AlO_x, and an aluminum oxyhydroxide phase (Al-O-OH). The differences in BE (see table in 3(b)) were found to be consistent across the measured chips and sites. The higher BE of the oxide components (~74.2 eV) for the untreated and annealed-only devices suggests the formation of an oxygen-rich aluminum oxide on their surface [27–29]. Additionally, the untreated chip shows a relatively strong Al-O-OH component (BE = ~75.55 eV), which is commonly found at the surface of Al exposed to wet environments. Annealing removes most of those Al-O-OH groups, while ALE+ALD removes all of them. Furthermore, we find that the ALE+ALD-treated chip has the thinnest oxide layer (2.52 ± 0.05 nm), followed by the native oxide of the Al blanket film (2.77 ± 0.03 nm), and then the untreated and annealed-only (3.1 ± 0.01 nm) chips. The thinning of the surface oxide layer of Al af-

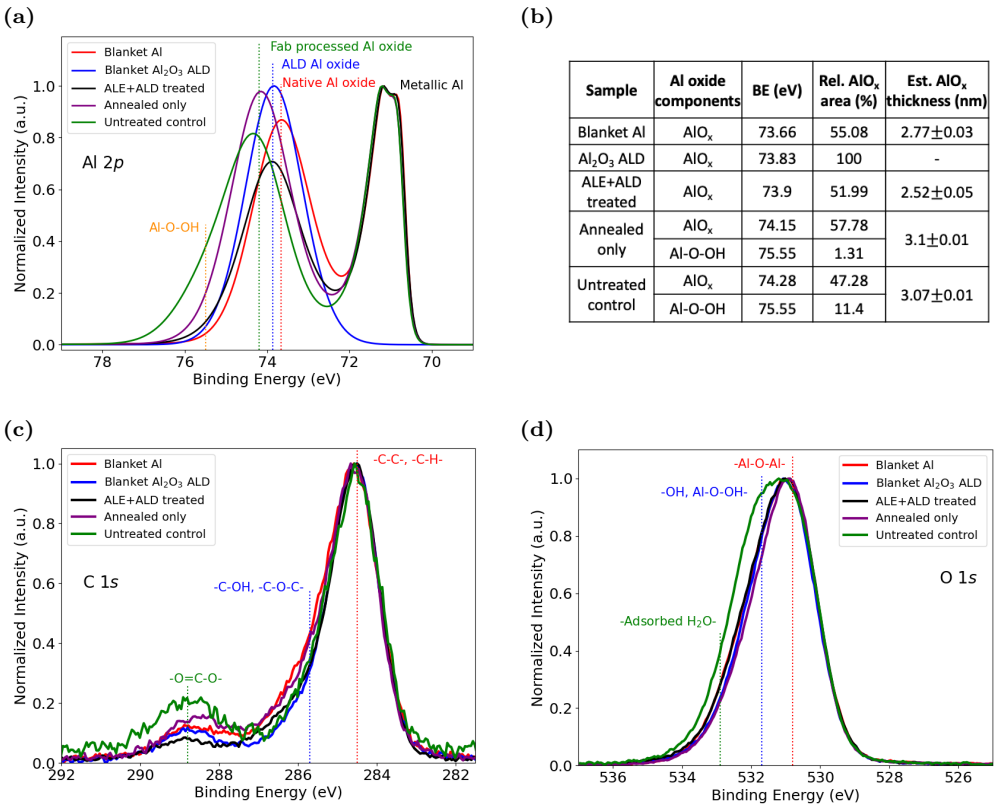

Sample	Al oxide components	BE (eV)	Rel. AlO_x area (%)	Est. AlO_x thickness (nm)
Blanket Al	AlO_x	73.66	55.08	2.77±0.03
Al_2O_3 ALD	AlO_x	73.83	100	-
ALE+ALD treated	AlO_x	73.9	51.99	2.52±0.05
Annealed only	AlO_x	74.15	57.78	3.1±0.01
	Al-O-OH	75.55	1.31	
Untreated control	AlO_x	74.28	47.28	3.07±0.01
	Al-O-OH	75.55	11.4	

FIG. 3. Al 2p (a), C 1s (c), and O 1s (d) core-level XPS spectra measured on reference blanket films and transmon qubit chips. The spectra in (a) are aligned in energy and normalized in intensity to the metallic Al 2p3/2 peak at $\sim$ 70.8 eV, and in (c) and (d) they are calibrated to the C-C bonding feature at 285.5 eV. Dashed lines highlight the different oxidation states and chemical bonds inferred from the relative energy shifts. Information inferred from the deconvolution of the experimental spectra is summarized in the table shown in (b).

ter ALE+ALD was confirmed by TEM-EELS, see Figure SI-7. The fact that the surface oxide in the ALE+ALD treated chip is thicker than the anticipated 1-nm thick ALD-grown layer can be attributed to the partial re-growth of a native-oxide layer during the 20 seconds that the sample spends at 300°C in the 6-7 Torr atmosphere of the process chamber upon completion of the ALE step and prior to the start of the ALD process[30].

The deconvolution of the C 1s core level reveals three distinct chemical environments of carbon, which, in order of increasing BE, are: adventitious carbon or -C-C- bonding, -C-OH- or -C-O-C- bonding, and -O=C-O- bonding. The decrease of the two latter components after annealing, but especially after ALE+ALD where their relative intensity is even weaker than in blanket Al, points to a reduction of organic species primarily stemming from residual resist contamination. The clear broadening of the O 1s peak observed in the untreated chip surface can be assigned to a contribution from adsorbed hydroxyl species such as Al-O-OH or $Al(OH)_3$ around 531.7 eV and adsorbed H_2O near 533 eV. These features are not observed after annealing or ALE+ALD treatment, which is consistent with the Al 2p data. Taken together, the XPS data shows that the ALE+ALD treatment results in a thinner and stoichiometric surface layer of Al_2O_3 with minimal polymeric contamination.

In order to gain spatially-resolved insights into this surface modification, we used PiFM to collect infrared spectroscopic data in the 800-1800 cm^{-1} range with a $\sim$10 nm lateral resolution. Areas of a few μm^2 centered around the junction and a portion of the Al/Si sidewall from a readout resonator were measured on untreated and ALE+ALD treated qubit chips. To introduce the spectroscopic features detected on the surface of our samples, we show the PiFM spectra averaged over the Si and Al regions of these measured areas in Figure 4(a). The spectra are normalized to their maximum values and offset along the y-axis to improve visibility between the two samples. Dashed lines serve as visual guides for the wavenumbers of peaks present either before and after the treatment (blue) or only after the treatment (red), respectively. A detailed peak assignment is provided in Table 2 in the SI. In the untreated chip, the signal measured across all areas is dominated by spectral features assigned to poly(methyl methacrylate) (PMMA, blue dashed lines in Figure 4) [31, 32], which is a resist used during liftoff and dicing steps of our fabrication flow. Despite soaking the chips in a heated solution of

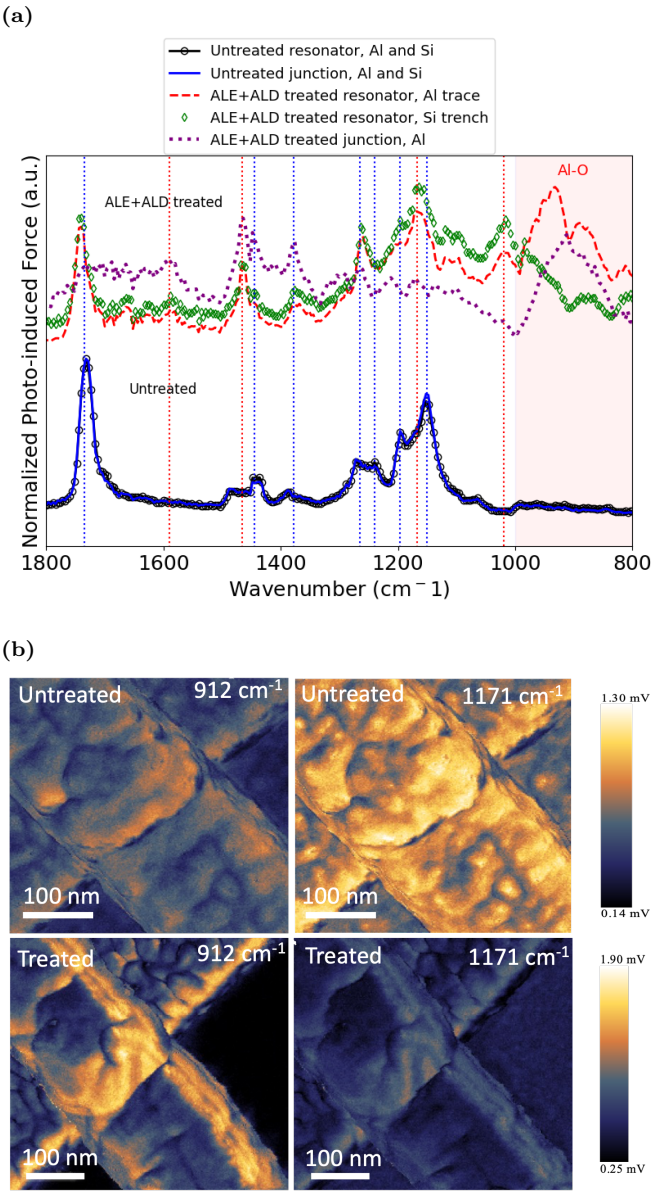

FIG. 4. (a) Comparison of PiFM spectra averaged across Si and Al regions of the areas measured on the untreated and ALE+ALD-treated transmon qubit chips, and normalized to their maxima. The blue dashed lines indicate peaks associated with PMMA and (b) PiFM maps at the JJ area shown with a color scale highlighting the 912 cm^{-1} and 1171 cm^{-1} wavenumbers, which respectively correspond to Al-O bonds and organic C-H bending and/or CH_3 deformation

N-methyl pyrrolidone (NMP) followed by an acetone and isopropyl alcohol rinse to strip the PMMA, the absence of a signal from AlO_x suggests that sufficient residual PMMA remains to form a continuous layer of at least ∼2 nm thickness on the untreated surface. This lower bound on the residual PMMA thickness is derived from tests conducted to estimate the minimum thickness of a thin polymer layer that can effectively shield the infrared signal from the underlying sample.

Conversely, we observe a broad absorbance feature around 850-1000 cm^{-1} assigned to Al-O stretching vibrations [33, 34] on both the resonator and junction areas of the ALE+ALD treated chip. A peak corresponding to C-O stretching vibrations also appears at 1020 cm^{-1} in the resonator area, suggesting PMMA decomposition. Previous studies showed that, at elevated temperatures, PMMA degrades into its monomer, MMA, which shares similar infrared features and can further undergo random scission around 300°C, breaking ester bonds into smaller fragments like C–O [35, 36]. Additionally, we find that the characteristic PMMA absorbance features are weaker in the resonator area and nearly suppressed in the junction area, indicating a significant reduction in the overall PMMA contamination. The cleaner junction surface can be attributed to the fewer exposures of the junction to MMA- and PMMA-containing resists compared to the ground plane, resulting in a thinner contamination layer and a more effective removal.

Alongside these changes, we observe new peaks around 1170 cm^{-1}, 1470 cm^{-1}, and 1590 cm^{-1}, marked with red dashed lines. We respectively identify these as C-H bending vibrations from Al-CH_3 bonds, asymmetric CH_3 bending deformation, and bending vibration of adsorbed water molecules, all of which have been previously reported during the ALD or ALE reactions involving trimethylaluminum (TMA) as one of the precursors [33, 37–42]. As anticipated from the selectivity of Al_2O_3 growth in the nucleation regime, no distinct absorption corresponding to Al-O stretching in the 850-1000 cm^{-1} range is observed in the Si trench area. The absence of Al_2O_3 capping on the Si surface after the ALE+ALD treatment was also confirmed by TEM-EELS map, as seen in Figure SI-7(e).

The effectiveness of the ALE+ALD treatment in reducing PMMA contamination on both Al and Si surfaces despite the intended selectivity of our ALE chemistry for AlO_x may seem surprising. The strong adhesion of PMMA to aluminum and silicon oxides has been previously attributed to the bonding between PMMA and the surface hydroxyl groups [43, 44]. The annealing-induced removal of hydroxyl bonds, suggested by the Al $2p$ and O $1s$ XPS data for the annealed-only chips, is expected to substantially weaken the adhesion of PMMA to both Al and Si surfaces, making it easier for the HF used in the ALE chemistry to indiscriminately etch the PMMA away. The degradation of PMMA at the ALE process temperature (300°C) [45], as described above, is also anticipated to ease the etch.

Figure 4(b) presents maps of the PiFM intensity collected at 912 cm^{-1} and 1171 cm^{-1} in the junction area for both untreated and ALE+ALD treated chips. Different scale bars are used to help highlight contrasts. The map at 912 cm^{-1} gains intensity from the Al-O stretching vibration, while the map at 1171 cm^{-1} does so from a mixture of C-O-C stretching vibration from PMMA and CH_3 bending deformation from the ALE/ALD chemistry. The ALE+ALD treatment causes the Al-O related sig-

nal to increase and the carbon-related signal to decrease, in a mostly uniform manner. A similar observation is made in the resonator area, as shown in Figure SI-8, which illustrates the overall uniformity of the ALE+ALD treatment across different regions and features within the chip. At a more local scale, we notice dark spots in the post-treatment maps that may correspond to preferential oxide regrowth during the nucleation growth regime.

D. Discussion

We have shown that post-fabrication ALE and ALD processes can significantly enhance the performance of Al-based CPW resonators and planar transmon chips, leading to a halving of dielectric loss in resonators and a two-fold enhancement in coherence times of planar transmons. 90^{th} percentile Q and T_1 values of 6 M and 320 μs at 3 GHz, respectively, have been achieved with this treatment. To our knowledge, these represent the longest reported coherence times for Al-based transmon qubits with compact dimensions aimed at scalability. Our approach of integrating post-fabrication surface treatment, in which ALE cleans all exposed surfaces and ALD encapsulates both the top surface and sidewalls of metal, differs from other recently reported methods that mitigate TLS loss by capping the ground metal top surface before etching[13–17]. Additionally, its compatibility with Al sets it apart from end-of-line wet chemical processes, such as BOE or tri-acid treatments, which are primarily used to reduce TLS loss mainly in Ta- or Nb- based superconducting devices.

Coherence improvement typically arises from two main factors: changes in the coupling strength of TLS to the transmon and a reduction in the TLS density or the material-based loss tangent. Assuming TLS couple to the transmon via an electric dipole, this coupling is determined by the electric field at the TLS. In our study, we compared T_1 enhancement in identical transmon designs before and after the treatment, ensuring that the electric field distribution of the transmon mode remains unchanged, and thus the coupling strength should also remain constant. This confirms that the observed two-fold increase in T_1 and Q results from a reduction in the weakly coupled TLS bath. This conclusion aligns with the measured resonator loss tangent, which also decreased by half after the treatment. The comparable improvement observed in both the resonator and transmon Q further suggests that the coherence ceiling in our transmons is predominantly limited by weakly coupled TLS defects located on the surfaces of the transmon capacitor pads. This reduction in the TLS density is reflected in the increased T_1, enabling us to reach a 90th percentile value of T_1 as high as 320 μs. However, the T_1 floor remains unchanged due to the finite population of weakly or intermediately coupled TLSs still present on the capacitor pads. This phenomenon accordingly results in an increased standard deviation in the measured T_1 and Q after the treatment.

We find that ALE+ALD treated surfaces exhibit a reduction in polymeric residues, along with a cleaner and more stoichiometric surface dielectric layer. In this work, we tested the effect of ALD-grown Al_2O_3 as the surface capping material observing a two-fold improvement in transmon coherence. While our study does not disentangle the individual contributions of polymeric residue removal and Al oxide layer modification, it establishes a direct correlation between improved material quality at the MA and SA interfaces and increased coherence times. Our findings suggest several pathways for future optimization of our process. These include incorporating a step in the ALE process to remove the silicon oxide from the substrate surface, gaining a deeper understanding of the mechanism by which ALE etches organic contamination to further enhance process efficiency, exploring lower-loss dielectric coatings beyond Al_2O_3, and distinguishing the effects of surface cleaning from that of higher-quality dielectric capping layers on transmon coherence times. Furthermore, changes in junction resistance induced by high-temperature treatment can lead to Purcell-limited qubit coherence times, which should be carefully mitigated.

III. CONCLUSION

We have demonstrated that the coherence times of aluminum transmons can be systematically and durably increased by more than two-fold using a combination of ALE and ALD. These processes uniquely enable post-fabrication surface treatment by removing fabrication residues from all exposed surfaces and replacing the Al native oxide from the top surface and sidewalls with a conformal, stoichiometric Al_2O_3 layer. Another differentiator of this approach from other surface treatments is the full compatibility with aluminum, a rarity among commonly used native oxide etchants. The concurrent doubling of the quality factor in Al-based resonators and transmons subjected to the same ALE+ALD treatment suggests that the observed improvement primarily stems from a reduction in the density of coherence-limiting TLS defects located on the surface of the capacitor pads. These findings establish a clear correlation between TLS loss, transmon relaxation times, and the chemical composition and purity of the MA and SA interfaces. They also provide a framework for continued improvements in quantum device performance through controlled, conformal, and aluminum-compatible surface treatments.

IV. METHODS

A. Surface Treatment: ALE and ALD process

The ALE chemistry developed for this work relies on alternating exposures of hydrogen fluoride-pyridine (HF-

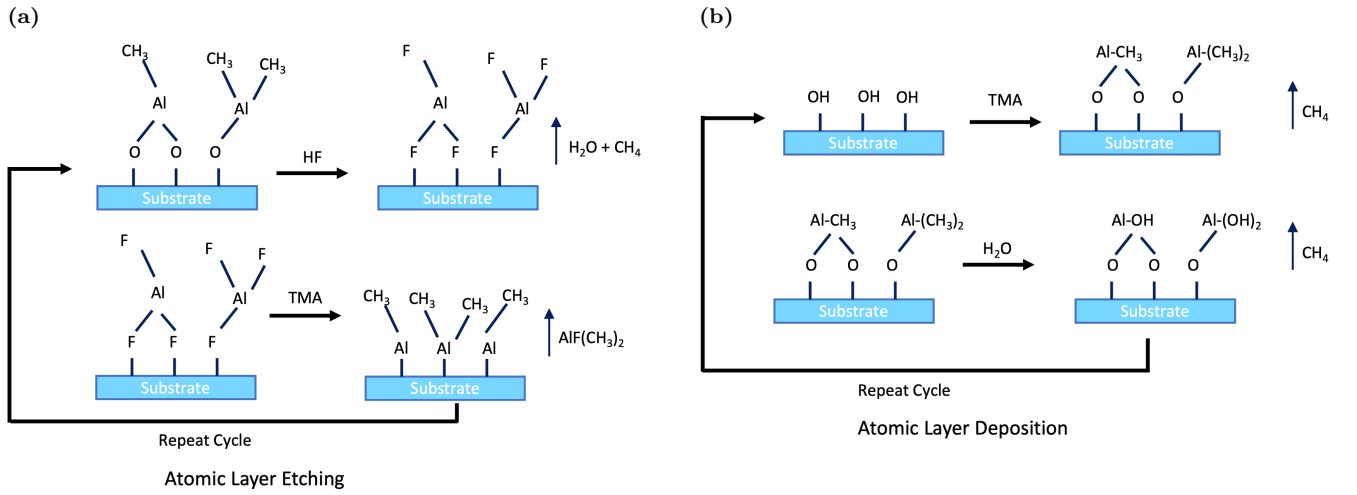

FIG. 5. Schematic representation of (a) ALE and (b) ALD using self-limiting surface chemistry and an AB binary reaction sequence.

pyridine) and TMA at 300°C resulting in an etch rate of 0.5 Å/cycle[46]. The reaction mechanism for the ALE of Al_2O_3 is depicted in Figure 5(a). The proposed two-half cycle reaction can be written as follows:

$$Al_2O_3^* + 6HF(g) \rightarrow 2AlF_3^* + 3H_2O(g) \uparrow \quad (2)$$

$$2AlF_3^* + 4Al(CH_3)_3(g) \rightarrow 6AlF(CH_3)_2(g) \uparrow \quad (3)$$

where the asterisk (*) denotes the surface species at the end of each half-cycle. In this ALE chemistry, HF reacts with the top few monolayers of Al_2O_3 to form AlF_3 in the first half cycle 'A' (equation (2)). In the second half cycles 'B' (equation (3)), AlF_3 is subsequently removed from the surface as $AlF(CH_3)_2$, a volatile species at 300°C, when reacted with TMA. Repetition of ABAB.. half cycles leads to the layer-by-layer etching.

Following the successful removal of the native Al oxide, the surface is encapsulated *in situ* with a thin layer of Al_2O_3 via ALD. The Al_2O_3 ALD process involves alternating exposures of TMA and water (H_2O)[47] at the same temperature of 300°C, resulting in a growth rate of 1 Å/cycle. This process begins immediately after the ALE to minimize spontaneous re-oxidation of the underlying Al surface. The reaction mechanism for the ALD of Al_2O_3 is depicted in Figure 5(b). The proposed two-half cycle reaction can be written as follows:

$$AlOH^* + Al(CH_3)_3(g) \rightarrow AlOAl(CH_3)_2^* + CH_4(g) \uparrow \quad (4)$$

$$AlOAl(CH_3)_2^* + H_2O(g) \rightarrow AlOH^* + CH_4(g) \uparrow \quad (5)$$

The ALD surface chemistry involves formation of Al-O-$Al(CH_3)_2$ surface species during the first half cycle 'C' (equation (4)) when Al-OH* surface species react with TMA. In the second half cycle 'D' (equation (5)), these species are converted back to Al-OH* when reacted with H_2O, ultimately leading to the formation of the Al_2O_3 monolayer on the surface.

The ALD and ALE processes were developed using a Picosun/AMAT R-200 tool at 300°C. Trimethlyaluminum (TMA) and HPLC grade water (H_2O) were used as the metal and the oxygen precursors for the Al_2O_3 ALD process while TMA and hydrogen fluoride-pyridine (HF-pyridine) served as the metal and fluorine sources for the etching of Al_2O_3. All the precursors were kept at room temperature. High purity nitrogen (N_2, 99.999% purity) was employed as the carrier gas to carry the precursors into the reaction chamber. The process base pressure was maintained at $\sim$ 11 hPa, with 300 sccm of N_2 directed into the chamber and $\sim$ 50 sccm of N_2 through all the precursor lines. The partial pressures of TMA, Al_2O_3 and HF-pyridine were maintained at 1.7 $\pm$ 0.2 hPa, 2.3 $\pm$ 0.2 hPa and 4 $\pm$ 0.5 hPa, respectively. N_2 was also used as a purge gas between successive doses of reactants. The optimized dosing sequence can be expressed as (t_1 - t_2 - t_3 - t_4), where t_1 is the dose time of TMA and t_3 is the dose time of Al_2O_3 or HF-pyridine, with t_2 and t_4 representing intermediate purge times. All the times are presented in seconds. The optimized dosing sequence for ALD Al_2O_3 was (0.2-10-0.2-10), while the dosing sequence for ALE Al_2O_3 was (1-10-1-10). Under these conditions, the etch rate of Al_2O_3 was measured to be $\sim$ 0.5 A/cycle, and the growth rate was $\sim$ 0.9 A/cyl. The combined ALE+ALD process includes 50 cycles of Al_2O_3 ALE, followed by 10 cycles of Al_2O_3 ALD at 300C. The combined recipe was applied to individual resonator and transmon chips, enabling the *in situ* removal of native Al oxide followed by encapsulation with $\sim$ 1 nm of ALD Al_2O_3 without breaking the vacuum.

B. Device Fabrication

The 2D transmons and resonators were fabricated on high-resistivity silicon wafers, beginning with a 10-minute oxygen plasma clean at 150 W in a Tergio Asher. The first step was to deposit aluminum ground layer. The lift-off ground layer process involved with spin coating of an adhesion promoter (SurPass 3000) and resist (ma-N 2403) and baking at 90°C, followed by electron beam (e-beam) lithography and development using ma-D 525. Before depositing 100 nm Al layer with 10 Å/s growth rate at 10^{-09} torr of base pressure in an Angstrom e-beam evaporator, the wafers were treated with 10-second oxygen direct plasma and 15-second of 10:1 BOE treatment. The lift-off process was completed by soaking the wafers in hot NMP solution at $\sim$ 150°C for 2 hours followed by thorough IPA and acetone rinses.

As a second layer of JJ deposition, the patterned Al was exposed to a 5-minute oxygen plasma treatment. This was followed by a combination of pre-bake and post bake steps and spin coating of bi-layer resists (MMA EL11 and PMMA A4 950K) at 170°C. After e-beam lithography and cold development in a 3:1 IPA:H2O solution at 1.6°C, the wafers underwent 5-second oxygen plasma treatment and a plasma ashing to etch $\sim$ 10 nm of resist. The wafers were then exposed to vapor HF treatment for 5 minutes and loaded into an Angstrom e-beam double angle evaporator for junction deposition with 10 Å/s growth rate at 10^{-09} torr of base pressure, using 60° and 0° angles for top down deposition. Finally, the resist was removed by a 2-hour hot NMP treatment at $\sim$ 150°C, followed by IPA and acetone rinses, and 10-minute oxygen plasma treatment to remove the residual photoresist.

Scaffold oxide features were fabricated in the next step by exposing the wafers to a 10-minute oxygen plasma treatment, followed by pre-bake and post-bake steps for spin coating a tri-layer resist (PMMA A4 950K, PMGI SF11 and ZEP 520a) at 182°C. After e-beam lithography, the wafers were developed in three solutions (ZED-N50, MF-319 and 3:1 IPA : H2O mixture), followed by a 30-second oxygen ashing in Oxford etcher. A 1 μm SiO_2 layer was deposited using an Angstrom evaporator at 1 Å/sec growth rate at $< 10^{-06}$ torr of base pressure. The oxide layer was lifted off in a 2-hour hot NMP treatment at 150°C, followed by IPA and acetone rinses and a final 10-minute oxygen plasma treatment. For the Al airbridges as the final fabrication layer, the same process was used, replacing the SiO_2 deposition with in situ pre-deposition ion milling and 400 nm of Al deposition in an Angstrom e-beam evaporator at 10 Å/s growth rate at 10^{-09} torr of base pressure.

As a final step, the wafers underwent a 10-minute oxygen plasma treatment and PMMA EL11 resist coating at 182°C. The wafers were then diced using an ADT dicing saw, UV cured for $\sim$ 7 minutes, and sorted. After dicing, the resist was removed with a 10-minute hot NMP bath at 150°C, followed by IPA and acetone rinses and 10-minute oxygen plasma treatment. Vapor HF treatment removed the scaffold oxide, releasing the airbridges, and completing the fabrication. The devices were then either subjected to ALE+ALD treatment or left untreated as control samples before mounting on the PCB for wire-bonding.

C. Resonator and Transmon Measurement

Measurements were conducted using a vector network analyzer (VNA) in a conventional set up to capture the S_{21} transmission of the resonators in a dilution refrigerator (DR) with a base temperature of 10 mK. The input lines consists of 75 dB total input attenuation and output line consists of a high electron mobility transistor (HEMT) amplifier at 4K stage and a room temperature amplifier.

To measure the resonator internal loss, we implemented a parameter-constrained diameter correction method (PC-DCM)[48], which reduces the parameter space in resonator data fitting and the uncertainty in the fitting result. Key parameters such as the coupling quality factor (Q_c) and impedance mismatch angle (ϕ) are extracted from high-power measurements and fixed for low-power analysis, improving fitting efficiency and robustness. For low-power measurements, we reduced the S_{21} frequency span to within one line-width of the resonance.

The quality factors reported in this study are based on measurements across three resonators on two devices for both untreated control and ALE+ALD-treated samples. The TLS-induced loss ($\delta_{TLS} = \frac{1}{Qtls}$) is derived from the quality factors measured at low power ($1/Q_{i,LP}$, collected at 1 photon or less) and high power ($1/Q_{i,HP}$) as $\delta_{TLS} = \frac{1}{Q_{TLS}} = \frac{1}{Q_{i,LP}} - \frac{1}{Q_{i,HP}}(1)$.

Similar to the resonator measurements, qubit measurements were conducted using the same setup in a dilution refrigerator (DR) at a base temperature of 10 mK. Further details on packaging and the cryogenic setup can be found elsewhere[49]. T_1 and T_2 were estimated by fitting an exponential decay to the inversion recovery[50, 51] and an exponentially decaying sinusoidal to the Ramsey curve[51], respectively, with each operating point measured for at least 3 hours. The transmon quality factor $Q = 2\pi f_{01} T_1$, where f_{01} is the qubit frequency. The measured anharmonicity was within 10% of the design value, which is approximately 220 MHz for all transmons. Notably, the anharmonicity remained unchanged after both ALE+ALD treatment and annealing. We measured transmon decoherence at various flux points away from the sweet spot (zero flux) over a frequency range of 1.0 to 1.5 GHz from the design value. While the designed qubit frequencies were initially between 4 and 5.5 GHz, factors such as junction energy mis-targeting due to fabrication variabilities, high-temperature annealing effects, and T_1 measurements taken off the sweet spot shifted the qubit

frequencies to 2.5–5 GHz.

D. Materials Characterization

XPS was performed using a Scienta Omicron instrument, with Casa XPS software employed for peak fitting and data analysis. The experimental conditions for XPS data acquisition utilized a 300 W Al x-ray source (λ = 1486.6 eV) under ultra-high vacuum (UHV) conditions (10^{-10} mbar), focussing on a spot size of $\sim 400\,\mu$m while collecting photoelectrons at a normal incidence angle to the sample surface and the detector. The acquired spectra were calibrated using the carbon peak at 284.5 eV.

Photo-induced force infrared microscopy (PiFM) measurements were performed at room temperature in air using a VistaScope (Molecular Vista Inc.) system, coupled with a LaserTune QCL. The system covered an infrared spectral range from 760 to 1800 cm^{-1} with a spectral resolution of 4 cm^{-1}. Data processing and analysis were carried out using SurfaceWorks software (Molecular Vista Inc.).

The morphology, surface oxide thickness, and elemental distribution at the Al and Si interfaces in the resonator and junction areas of our transmon devices, both untreated and ALE+ALD treated, were imaged using scanning transmission electron microscopy and electron energy loss spectroscopy (STEM-EELS). Samples were prepared via a focused ion beam (FIB) lift-out technique, using spin-on polymer (SOP) and electron-beam deposited platinum (e-Pt) before milling. The lamella thickness was approximately 70 nm. Measurements were performed on an FEI probe-corrected TITAN operated at 200 kV, in bright-field STEM and Z-contrast high-angle annular dark-field (HAADF) STEM modes, achieving a resolution of $\sim$0.78 Å.

V. ACKNOWLEDGEMENTS

We thank the staff from across the AWS Center for Quantum Computing that enabled this project. We also thank Simone Severini, Bill Vass, James Hamilton, Nafea Bshara, and Peter DeSantis at AWS for their involvement and support of the research activities at the AWS Center for Quantum Computing.

[1] G. Wendin, "Quantum information processing with superconducting circuits: a review," Reports on Progress in Physics, vol. 80, no. 10, p. 106001, 2017.

[2] J. M. Martinis, "Surface loss calculations and design of a superconducting transmon qubit with tapered wiring," npj Quantum Information, vol. 8, no. 1, p. 26, 2022.

[3] S. Eun, S. H. Park, K. Seo, K. Choi, and S. Hahn, "Shape optimization of superconducting transmon qubits for low surface dielectric loss," Journal of Physics D: Applied Physics, vol. 56, no. 50, p. 505306, 2023.

[4] C. E. Murray, "Material matters in superconducting qubits," Materials Science and Engineering: R: Reports, vol. 146, p. 100646, 2021.

[5] A. P. Place, L. V. Rodgers, P. Mundada, B. M. Smitham, M. Fitzpatrick, Z. Leng, A. Premkumar, J. Bryon, A. Vrajitoarea, S. Sussman, et al., "New material platform for superconducting transmon qubits with coherence times exceeding 0.3 milliseconds," Nature communications, vol. 12, no. 1, p. 1779, 2021.

[6] A. Premkumar, C. Weiland, S. Hwang, B. Jäck, A. P. Place, I. Waluyo, A. Hunt, V. Bisogni, J. Pelliciari, A. Barbour, et al., "Microscopic relaxation channels in materials for superconducting qubits," Communications Materials, vol. 2, no. 1, p. 72, 2021.

[7] C. Wang, X. Li, H. Xu, Z. Li, J. Wang, Z. Yang, Z. Mi, X. Liang, T. Su, C. Yang, et al., "Towards practical quantum computers: Transmon qubit with a lifetime approaching 0.5 milliseconds," npj Quantum Information, vol. 8, no. 1, p. 3, 2022.

[8] J. Biznárová, A. Osman, E. Rehnman, L. Chayanun, C. Križan, P. Malmberg, M. Rommel, C. Warren, P. Delsing, A. Yurgens, et al., "Mitigation of interfacial dielectric loss in aluminum-on-silicon superconducting qubits," npj Quantum Information, vol. 10, no. 1, p. 78, 2024.

[9] K. D. Crowley, R. A. McLellan, A. Dutta, N. Shumiya, A. P. Place, X. H. Le, Y. Gang, T. Madhavan, M. P. Bland, R. Chang, et al., "Disentangling losses in tantalum superconducting circuits," Physical Review X, vol. 13, no. 4, p. 041005, 2023.

[10] C. J. Kopas, D. P. Goronzy, T. Pham, C. G. Torres Castanedo, M. Cheng, R. Cochrane, P. Nast, E. Lachman, N. Z. Zhelev, A. Vallières, et al., "Enhanced superconducting qubit performance through ammonium fluoride etch," Materials for Quantum Technology, 2024.

[11] D. Lozano, M. Mongillo, X. Piao, S. Couet, D. Wan, Y. Canvel, A. Vadiraj, T. Ivanov, J. Verjauw, R. Acharya, et al., "Low-loss α-tantalum coplanar waveguide resonators on silicon wafers: fabrication, characterization and surface modification," Materials for Quantum Technology, vol. 4, no. 2, p. 025801, 2024.

[12] M. Alghadeer, A. Banerjee, A. Hajr, H. Hussein, H. Fariborzi, and S. G. Rao, "Surface passivation of niobium superconducting quantum circuits using self-assembled monolayers," ACS applied materials & interfaces, vol. 15, no. 1, pp. 2319–2328, 2022.

[13] C. Zhou, J. Mun, J. Yao, A. k. Anbalagan, M. D. Hossain, R. A. McLellan, R. Li, K. Kisslinger, G. Li, X. Tong, et al., "Ultrathin magnesium-based coating as an efficient oxygen barrier for superconducting circuit materials," Advanced Materials, vol. 36, no. 18, p. 2310280, 2024.

[14] R. D. Chang, N. Shumiya, R. A. McLellan, Y. Zhang, M. P. Bland, F. Bahrami, J. Mun, C. Zhou, K. Kisslinger, G. Cheng, et al., "Eliminating surface oxides of superconducting circuits with noble metal encapsulation," arXiv preprint arXiv:2408.13051, 2024.

[15] M. Bal, A. A. Murthy, S. Zhu, F. Crisa, X. You, Z. Huang, T. Roy, J. Lee, D. v. Zanten, R. Pilipenko,

et al., "Systematic improvements in transmon qubit coherence enabled by niobium surface encapsulation," npj Quantum Information, vol. 10, no. 1, p. 43, 2024.

[16] S. K. Karuppannan, D. Huang, N. M. Kommanaboina, K. Anil, G. Yan, D. V. M. Repaka, Y. Zhang, K. E. J. Goh, W. S. Kai, N. L. Chee Beng, et al., "Improved interface of niobium superconducting resonator with ruthenium as a capping layer," ACS Applied Electronic Materials, 2024.

[17] M. C. de Ory, D. Rodriguez, M. T. Magaz, V. Rollano, D. Granados, and A. Gomez, "Low loss hybrid nb/au superconducting resonators for quantum circuit applications," arXiv preprint arXiv:2401.14764, 2024.

[18] W. Woods, G. Calusine, A. Melville, A. Sevi, E. Golden, D. K. Kim, D. Rosenberg, J. L. Yoder, and W. D. Oliver, "Determining interface dielectric losses in superconducting coplanar-waveguide resonators," Physical Review Applied, vol. 12, no. 1, p. 014012, 2019.

[19] C. R. H. McRae, H. Wang, J. Gao, M. R. Vissers, T. Brecht, A. Dunsworth, D. P. Pappas, and J. Mutus, "Materials loss measurements using superconducting microwave resonators," Review of Scientific Instruments, vol. 91, no. 9, 2020.

[20] G. Marcaud, D. Perello, C. Chen, E. Umbarkar, C. Weiland, J. Gao, S. Diez, V. Ly, N. Mahuli, N. D'Souza, et al., "Low-loss superconducting resonators fabricated from tantalum films grown at room temperature," arXiv preprint arXiv:2501.09885, 2025.

[21] P. G. Baity, C. Maclean, V. Seferai, J. Bronstein, Y. Shu, T. Hemakumara, and M. Weides, "Circle fit optimization for resonator quality factor measurements: Point redistribution for maximal accuracy," Physical Review Research, vol. 6, no. 1, p. 013329, 2024.

[22] Q.-M. Chen, M. Pfeiffer, M. Partanen, F. Fesquet, K. E. Honasoge, F. Kronowetter, Y. Nojiri, M. Renger, K. G. Fedorov, A. Marx, et al., "Scattering coefficients of superconducting microwave resonators. i. transfer matrix approach," Physical Review B, vol. 106, no. 21, p. 214505, 2022.

[23] G. Calusine, A. Melville, W. Woods, R. Das, C. Stull, V. Bolkhovsky, D. Braje, D. Hover, D. K. Kim, X. Miloshi, et al., "Analysis and mitigation of interface losses in trenched superconducting coplanar waveguide resonators," Applied Physics Letters, vol. 112, no. 6, 2018.

[24] R. Barends, J. Kelly, A. Megrant, D. Sank, E. Jeffrey, Y. Chen, Y. Yin, B. Chiaro, J. Mutus, C. Neill, et al., "Coherent josephson qubit suitable for scalable quantum integrated circuits," Physical review letters, vol. 111, no. 8, p. 080502, 2013.

[25] C. Y. H. Carruzzo, "Two-level systems and the tunneling model: A critical view,(2021)," arXiv preprint ArXiv:2101.02787.

[26] J. M. Gambetta, C. E. Murray, Y.-K.-K. Fung, D. T. McClure, O. Dial, W. Shanks, J. W. Sleight, and M. Steffen, "Investigating surface loss effects in superconducting transmon qubits," IEEE Transactions on Applied Superconductivity, vol. 27, no. 1, pp. 1–5, 2016.

[27] S. Prasanna, G. Krishnendu, S. Shalini, P. Biji, G. M. Rao, S. Jayakumar, and R. Balasundaraprabhu, "Composition, structure and electrical properties of dc reactive magnetron sputtered al2o3 thin films," Materials science in semiconductor processing, vol. 16, no. 3, pp. 705–711, 2013.

[28] N. Reddy, P. Bera, V. R. Reddy, N. Sridhara, A. Dey, C. Anandan, and A. K. Sharma, "Xps study of sputtered alumina thin films," Ceramics International, vol. 40, no. 7, pp. 11099–11107, 2014.

[29] G. A. Mengesha, J. P. Chu, B.-S. Lou, and J.-W. Lee, "Corrosion performance of plasma electrolytic oxidation grown oxide coating on pure aluminum: effect of borax concentration," Journal of Materials Research and Technology, vol. 9, no. 4, pp. 8766–8779, 2020.

[30] L. Nguyen, T. Hashimoto, D. N. Zakharov, E. A. Stach, A. P. Rooney, B. Berkels, G. E. Thompson, S. J. Haigh, and T. L. Burnett, "Atomic-scale insights into the oxidation of aluminum," ACS applied materials & interfaces, vol. 10, no. 3, pp. 2230–2235, 2018.

[31] S. B. Aziz, O. G. Abdullah, M. Brza, A. K. Azawy, and D. A. Tahir, "Effect of carbon nano-dots (cnds) on structural and optical properties of pmma polymer composite," Results in Physics, vol. 15, p. 102776, 2019.

[32] G. Duan, C. Zhang, A. Li, X. Yang, L. Lu, and X. Wang, "Preparation and characterization of mesoporous zirconia made by using a poly (methyl methacrylate) template," Nanoscale research letters, vol. 3, pp. 118–122, 2008.

[33] D. N. Goldstein, J. A. McCormick, and S. M. George, "Al2o3 atomic layer deposition with trimethylaluminum and ozone studied by in situ transmission ftir spectroscopy and quadrupole mass spectrometry," The Journal of Physical Chemistry C, vol. 112, no. 49, pp. 19530–19539, 2008.

[34] V. Vemuri, S. W. King, W. A. Lanford, J. T. Gaskins, P. E. Hopkins, J. Van Derslice, H. Li, and N. C. Strandwitz, "Comprehensive study of the chemical, physical, and structural evolution of molecular layer deposited alucone films during thermal processing," Chemistry of Materials, vol. 35, no. 5, pp. 1916–1925, 2023.

[35] T. Kashiwagi, A. Inabi, and A. Hamins, "Behavior of primary radicals during thermal degradation of poly (methyl methacrylate)," Polymer Degradation and Stability, vol. 26, no. 2, pp. 161–184, 1989.

[36] L. E. Manring, "Thermal degradation of poly (methyl methacrylate). 4. random side-group scission," Macromolecules, vol. 24, no. 11, pp. 3304–3309, 1991.

[37] Y. Lee, J. W. DuMont, A. S. Cavanagh, and S. M. George, "Atomic layer deposition of alf3 using trimethylaluminum and hydrogen fluoride," The Journal of Physical Chemistry C, vol. 119, no. 25, pp. 14185–14194, 2015.

[38] J. W. DuMont and S. M. George, "Competition between al2o3 atomic layer etching and alf3 atomic layer deposition using sequential exposures of trimethylaluminum and hydrogen fluoride," The Journal of Chemical Physics, vol. 146, no. 5, 2017.

[39] B. Gong and G. N. Parsons, "Quantitative in situ infrared analysis of reactions between trimethylaluminum and polymers during al 2 o 3 atomic layer deposition," Journal of Materials Chemistry, vol. 22, no. 31, pp. 15672–15682, 2012.

[40] A. Yanguas-Gil, J. A. Libera, and J. W. Elam, "In situ ftir characterization of growth inhibition in atomic layer deposition using reversible surface functionalization," ECS Transactions, vol. 50, no. 13, p. 43, 2013.

[41] H. A. Al-Abadleh and V. Grassian, "Ft-ir study of water adsorption on aluminum oxide surfaces," Langmuir,

vol. 19, no. 2, pp. 341–347, 2003.

[42] T. Seki, K.-Y. Chiang, C.-C. Yu, X. Yu, M. Okuno, J. Hunger, Y. Nagata, and M. Bonn, "The bending mode of water: a powerful probe for hydrogen bond structure of aqueous systems," The journal of physical chemistry letters, vol. 11, no. 19, pp. 8459–8469, 2020.

[43] E. Papirer, J.-M. Perrin, G. Nanse, and P. Fioux, "Adsorption of poly (methylmethacrylate) on an α alumina: evidence of formation of surface carboxylate bonds," European polymer journal, vol. 30, no. 8, pp. 985–991, 1994.

[44] J. Watts, S. Leadley, J. Castle, and C. Blomfield, "Adsorption of pmma on oxidized al and si substrates: An investigation by high-resolution x-ray photoelectron spectroscopy," Langmuir, vol. 16, no. 5, pp. 2292–2300, 2000.

[45] M. Ferriol, A. Gentilhomme, M. Cochez, N. Oget, and J. Mieloszynski, "Thermal degradation of poly (methyl methacrylate)(pmma): modelling of dtg and tg curves," Polymer degradation and stability, vol. 79, no. 2, pp. 271–281, 2003.

[46] Y. Lee, J. W. DuMont, and S. M. George, "Trimethylaluminum as the metal precursor for the atomic layer etching of al2o3 using sequential, self-limiting thermal reactions," Chemistry of Materials, vol. 28, no. 9, pp. 2994–3003, 2016.

[47] R. L. Puurunen, "Surface chemistry of atomic layer deposition: A case study for the trimethylaluminum/water process," Journal of applied physics, vol. 97, no. 12, 2005.

[48] C. Chen, D. Perello, S. Aghaeimeibodi, G. Marcaud, I. Jarrige, H. Lee, W. Fon, M. Matheny, and J. Gao, "Efficient methods for extracting superconducting resonator loss in the single-photon regime," Journal of Applied Physics, vol. 137, no. 4, 2025.

[49] H. Levine, A. Haim, J. S. Hung, N. Alidoust, M. Kalaee, L. DeLorenzo, E. A. Wollack, P. Arrangoiz-Arriola, A. Khalajhedayati, R. Sanil, et al., "Demonstrating a long-coherence dual-rail erasure qubit using tunable transmons," Physical Review X, vol. 14, no. 1, p. 011051, 2024.

[50] Z. Wei, Y.-J. Ma, H. Jang, W. Yang, and J. Du, "To measure t1 of short t2 species using an inversion recovery prepared three-dimensional ultrashort echo time (3d irute) method: A phantom study," Journal of Magnetic Resonance, vol. 314, p. 106725, 2020.

[51] J. Montañez-Barrera, M. R. von Spakovsky, C. E. Damian Ascencio, and S. Cano-Andrade, "Decoherence predictions in a superconducting quantum processor using the steepest-entropy-ascent quantum thermodynamics framework," Physical Review A, vol. 106, no. 3, p. 032426, 2022.